

Full Length Article

Meso-silica/Erbium-doped ceria binary particles as functionalized abrasives for photochemical mechanical polishing (PCMP)

Ailian Chen^a, Yuhuan Duan^a, Zhaoyu Mu^b, Wenjie Cai^b, Yang Chen^{b,*}^a School of Mechanical Engineering, Changzhou University, Changzhou, Jiangsu 213016, PR China^b School of Material Science and Engineering, Changzhou University, Changzhou, Jiangsu 213016, PR China

ARTICLE INFO

Keywords:

Meso-silica
Er³⁺-doped ceria
Binary particle
Functionalized abrasive
Photochemical mechanical polishing (PCMP)

ABSTRACT

We report the design and synthesis of meso-silica/ceria binary composite particles and their usage as functionalized abrasives for photochemical mechanical polishing (PCMP). Meso-silica nanospheres were uniformly coated with (Er³⁺-doped) ceria nanoparticles via an environmentally friendly precipitation approach. The resulting products were characterized by XRD, FESEM, HRTEM, HADDF-STEM, EDX mapping, UV-vis, Raman, XPS, PL, and nitrogen adsorption-desorption measurements. High-resolution AFM analyses revealed that the binary abrasives contributed to mechanical damage and scratch eliminations, and finally achieved ultra-smooth surfaces with an average root-mean-square roughness of less than 0.2 nm. Owing to the increased oxygen vacancy and Ce³⁺ ion contents, the Er³⁺-doped abrasives in oxide-PCMP exhibited superior removal rates derived from the improved photocatalytic and tribochemical activities, thus leading to a 160% increment of removal rates compared to the undoped ones in oxide-CMP. The topographical variations of the surfaces after PCMP with Er³⁺-doped composites significantly reduced from ± 3.1 nm to ± 0.39 nm. High-quality and high-efficiency polishing can be achieved by the dynamical balance between the photocatalytic surface modification and the tribochemical material removal of the chemically soft layers. Furthermore, the synergistic roles of elastic meso-silica supports and active ceria components of the binary abrasives in material removal processes were also discussed.

1. Introduction

Photochemical mechanical polishing (PCMP) technique has been developed and introduced into the ultra-precision processing of hard and chemically inert materials (GaN, SiC, etc.), which commonly exhibit an extremely low material removal rate (*MRR*) in conventional chemical mechanical polishing (CMP). In typical photocatalytic oxidation-assisted CMP applications [1–5], the usage of ultraviolet (UV) radiation and photocatalyst create an increased concentration of the oxidation active species (hydroxyl radical ·OH, superoxide radical ·O₂[·], photo-induced hole h⁺) in polishing slurries. It can accelerate the formation of the oxidation modified layer on the substrate surfaces and result in a significantly enhanced *MRR*.

The type and property of the photocatalysts play a critical role in PCMP. For example, Wang and coworkers [1] investigated the GaN-PCMP performance of three N-type semiconductor nanoparticles (TiO₂, SnO₂, and Fe₂O₃) in H₂O₂-SiO₂-based slurries. It was found that the TiO₂ photocatalysts presented a superior photocatalytic activity and

achieved an improved *MRR*, possibly resulting from the relatively small particle size and narrow energy gap. Yuan and coworkers [3] reported that TiO₂ photocatalysts also exhibited an enhanced SiC-PCMP performance, and proposed that the SiC surface was firstly oxidized and soften by the generated ·OH, and then removed by SiO₂ particle abrasives. Recently, Yu and coworkers [5] explored the effects of ZnO, TiO₂, and ZrO₂ catalysts on the *MRR* in PCMP towards GaN materials. According to the current reports, the (SiO₂ + TiO₂) mixed nanoparticles are the most popular abrasive system in PCMP applications. In these cases, TiO₂ particles serve as photocatalysts and provide photocatalytic oxidation activity for surface modification, while SiO₂ particles act as polishing abrasives and offer the abrasion function for mechanical material removal.

In ultra-precision polishing applications, the flexible or soft abrasives with low modulus (*E*) and/or hardness contribute to the optimization of interfacial contact state and stress distribution, friction and wear, and material removal behavior [6,7]. Porous abrasives and core/shell abrasives commonly contribute to improving surface quality in

* Corresponding author.

E-mail address: 00001744@cczu.edu.cn (Y. Chen).

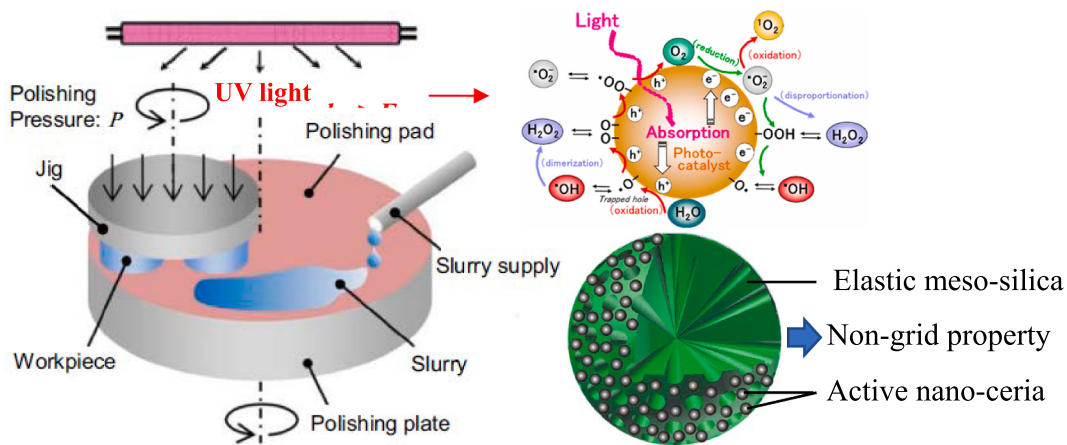


Fig. 1. Schematic view of the polishing experimental set-up.

conventional CMP [8], magnetic-field-assisted polishing [9], and electrochemical mechanical polishing (ECMP) [10,11]. Recently, Gao and coworkers [12] developed multicomponent polystyrene (PS)/CeO₂-TiO₂ core/shell abrasives for improved SiC-PCMP performance. Compared to conventional CeO₂ and CeO₂-TiO₂ abrasives, the novel composites achieved a reduced surface roughness and an enhanced MRR under UV irradiation. It was also proposed that the photo-induced h^+ could oxidize OH⁻/H₂O into the 'OH with powerful oxidation activity, which promoted the formation of an easily removed SiO₂ layer on the hard SiC surface. However, the particle morphology, size distribution, component, and core/shell structure controls over the PS/CeO₂-TiO₂ abrasives are still unsatisfactory. The ultra-precision polishing performance can be further improved by optimizing the structure and property of the composite abrasives.

Cerium oxide/ceria (CeO₂) materials simultaneously possess tribochemical activity [13,14] and photocatalytic activity [15,16], which are necessary for the abrasive system of PCMP. In this presented work, we designed and synthesized the binary core/shell composites containing the low-modulus meso-silica (mSiO₂) spheres and high-activity Er³⁺-doped CeO₂ nanoparticles. The purpose of the mSiO₂ is to improve surface quality, originating from the reduced overall modulus. And the aim of the Er³⁺-doping in CeO₂ is to improve polishing efficiency, resulting from their enhanced tribochemical and photocatalytic activities. The ionic radius of Er³⁺ is close to that of Ce⁴⁺ ions, and Er³⁺ is easily introduced into CeO₂ host lattice [17]. Furthermore, Er³⁺-doping contributed to the increase of oxygen vacancy and Ce³⁺ content in CeO₂ lattices [18]. The presented PCMP results clearly revealed that the CeO₂-based binary abrasives contributed the surface roughness and topographical variation reductions and the MRR enhancement. To the best of our knowledge, this is the first report about the design and optimization of functionalized CeO₂-based particle abrasives for PCMP applications.

2. Experimental details

2.1. Chemicals

Tetraethyl orthosilicate (TEOS), ammonia solution (NH₃·H₂O), ethanol, acetone, and sodium hydroxide (NaOH) were obtained from Shanghai Chemical Reagent Co., Ltd. (China). Cerium nitrate hexahydrate (Ce(NO₃)₃·6H₂O), erbium nitrate pentahydrate (Er(NO₃)₃·5H₂O), cetyltrimethylammonium bromide (CTAB), polyvinylpyrrolidone (PVP), and hexamethylenetetramine (HMT) were purchased from Shanghai Lingfeng Chemical Reagents Company. Deionized (DI) water was used throughout the experiments. All chemicals were of analytical grade and used without further purification.

2.2. Synthesis of mSiO₂ spheres and binary composites

Monodispersed mSiO₂ spheres were prepared by a modified Stöber method according to our previous work [19]. A typical procedure was described as follows. Firstly, CTAB (0.4 g), ammonia (1.8 g), ethanol (15.8 g), and DI water (100.0 g) were mixed and stirred magnetically (200–300 r/min) at 30 °C for 30 min. Subsequently, a mixture of TEOS (0.25 g) and ethanol (23.7 g) was added into the above solution. The resulting mixture was stirred magnetically at a relatively high speed of 800 r/min for 1 min, followed by stirring magnetically at a relatively low speed of 200–300 r/min for 2 h. Finally, the solid products were separated by repeated centrifugation, washed with DI water and ethanol several times, dried at 80 °C for 12 h, and annealed in air at 550 °C for 2 h.

For fabrication of binary particles, the as-obtained mSiO₂ powders (0.2 g) were dispersed in ethanol (23.7 g) with sonication for 10 min. Subsequently, a mixed aqueous solution containing Ce(NO₃)₃·6H₂O (0.3 g), HMT (0.5 g), and DI water (40.0 g) was added into the dispersion mentioned above. The resulting mixture was stirred (200–300 r/min) at 75 °C for 2 h. After the reaction, the obtained samples were collected by centrifugation (8000 r/min), washed, and then dried at 80 °C for 12 h. Finally, the resulting core/shell structured products were annealed in a muffle oven in air at 650 °C for 2 h, and the obtained mSiO₂/CeO₂ binary particles were named as Composite-A. For comparison, mSiO₂ cores were also grafted with Er³⁺-doped CeO₂ nanoparticles via a similar procedure as above except that 0.25 g of Ce(NO₃)₃·6H₂O and 0.05 g of Er (NO₃)₃·5H₂O were used. And the resulting mSiO₂/Ce_{0.83}Er_{0.17}O₂ particles were noted as composite-B. Additionally, the rigid SiO₂/CeO₂ composite particles were prepared using conventional solid silica cores (200–250 nm).

2.3. Characterization methods

The morphology, structure, and particle size of the resulting products were examined by a field emission scanning electron microscope (FESEM, SUPRA 55, Zeiss) and a transmission electron microscope (TEM, JEM-2100, JEOL). Powder X-ray diffraction (XRD) patterns were recorded on a Rigaku D/Max 2500 PC diffractometer. Nitrogen adsorption/desorption measurements were carried out on a Micromeritics TriStar 3020 apparatus. The pore size distribution and the specific area were calculated by the Barratt-Joyner-Halenda (BJH) and Brunauer-Emmett-Teller (BET) methods, respectively. X-ray photoelectron spectroscopy (XPS) analysis was conducted using a Thermo ESCALAB 250 spectrometer with Al K α radiation ($h\nu = 1486.6$ eV). High-angle annular dark field-scanning transmission electron microscopy (HAADF-STEM) image and EDX elemental mapping were performed on an FEI Talos 200S TEM system operated at an accelerating

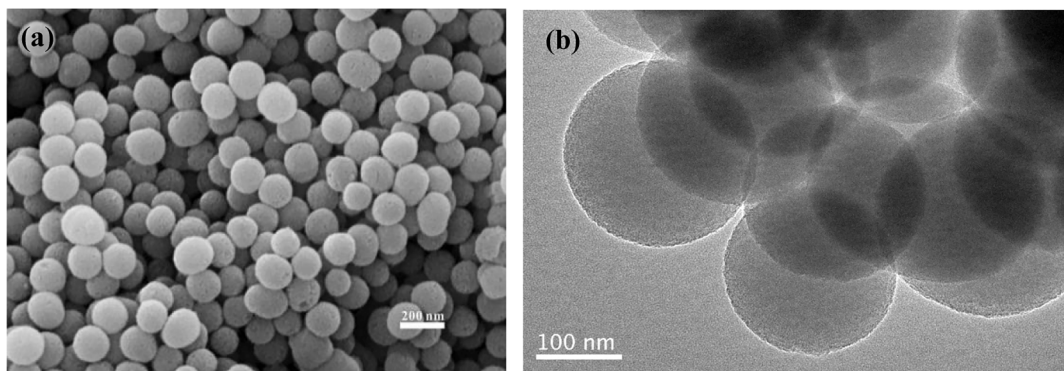


Fig. 2. FESEM (a) and TEM (b) images of mSiO₂ samples.

voltage of 300 kV. Raman spectra were recorded on a Raman microscope spectrometer (DXR, ThermoFisher). A diffuse reflectance ultra-violet-visible (UV-vis) spectrophotometer (UV-3600, Shimadzu) was used to obtain UV-vis spectra. Photoluminescence (PL) spectra were tracked using a fluorescence spectrophotometer (LS45, PEI).

2.4. Polishing experiments

For polishing slurry preparations, the composite abrasives (1 g), PVP (2 g), and DI water (100 g) were mixed and treated by sonication at room temperature for 20 min. The pH was adjusted to 8.5–9.0 by 0.1 M NaOH. Thermally grown silicon oxide wafers were supplied from Huacheng Changban Microelectronics Company (Changzhou, China) and cut into 2 cm × 2 cm pieces for polishing tests. A precision polishing machine (TegraForce-1/TrgraPol-15, Struers, Denmark) equipped with a polyurethane porous pad (MD-Chem, Struers, Denmark) was applied in conventional CMP and PCMP experiments. The platen rotation speed was 90 r/min, the carrier rotation speed was 120 r/min, the applied pressure was 3.3 psi, the polishing time was 2 min, and the slurry supplying rate was 100 mL/min. Schematic view of the polishing experimental set-up is shown in Fig. 1. A halogen lamp (250 W) was used as a UV source (365 nm of wavelength) in PCMP experiments.

The polished wafers were treated with ultrasonic cleaning in DI water and ethanol repeatedly, and then dried in a clean room. An atomic force microscope (AFM, Nanoman VS, Digital Instruments, equipped with a Dimension V controller) was employed to examine the surface topography and roughness within 5 μm × 5 μm aeras in tapping model with a scanning rate of 1 Hz and a sample/line of 256. Standard silicon probes (Tap300Al-G, BudgetSensors) with a typical resonant frequency of 300 kHz, a spring constant of 40 N/m, and a tip radius of less than 10

nm were utilized in all AFM measurements. An ultra-precision electron balance (XS105, Mettler Toledo, exact to 0.01 mg) was used for measuring workpiece weights. And the polishing efficiency or material removal rate (*MRR*, nm/min) was calculated by the following equation:

$$\text{MRR} = \frac{m_0 - m}{\rho \cdot s \cdot t} \quad (1)$$

where m_0 and m is the workpiece masses before and after polishing, ρ is the density of silicon oxide layer, s is the workpiece areas, and t is the polishing time. In this work, the presented *MRR* and roughness data were the average of three runs.

3. Results and discussion

3.1. Structural analyses of composite particles

The mSiO₂ morphologies were tracked by FESEM and TEM observations. Spherical and monodispersed mSiO₂ particles can be clearly observed from the FESEM image (Fig. 2a), and the particle size is 212 ± 8 nm (calculated from more than 20 individual particles). The corresponding TEM image (Fig. 2b) presents a relatively low electronic contrast, possibly resulting from their porous structures with worm-like radial meso-channels. The wide-angle XRD pattern (Fig. 3a) shows one peak near $2\theta = 23^\circ$, revealing the amorphous nature of the samples. The meso-channel organizations of the mSiO₂ were further examined by low-angle XRD. As shown in Fig. 3b, only one peak located at $2\theta = 2^\circ$ – 4° can be clearly tracked, suggesting the limited organizations of meso-pores with respect to typical SBA15 or MCM41 meso-silica materials [19].

The mSiO₂ samples exhibited typical type-IV isotherms (Fig. 4a), indicating the presence of well-defined mesopores. However, the

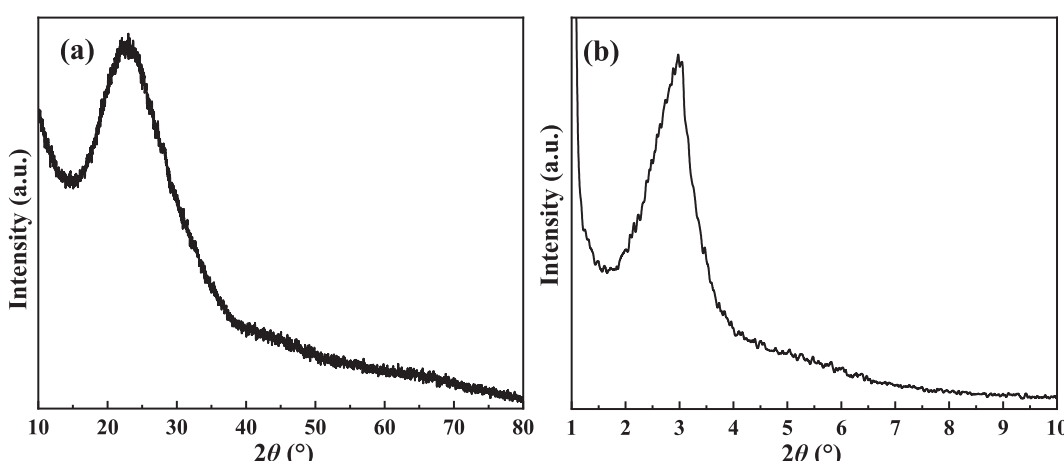


Fig. 3. Wide-angle (a) and low-angle (b) XRD patterns of mSiO₂ samples.

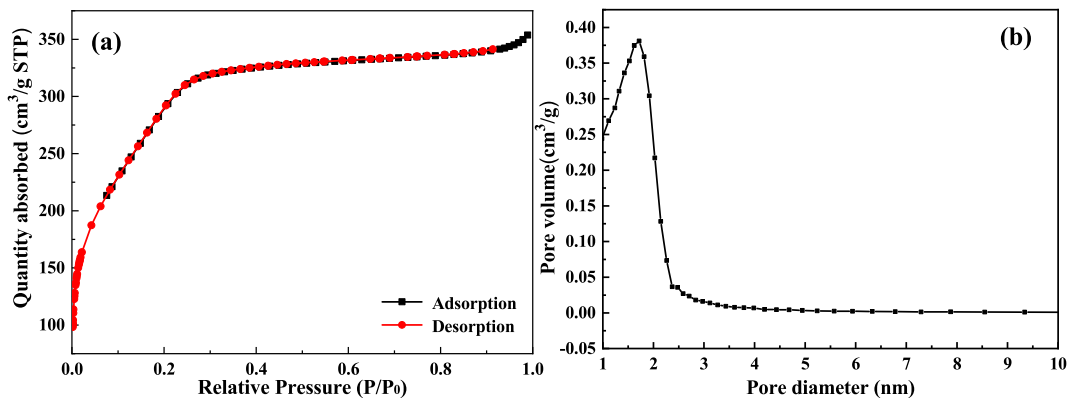


Fig. 4. N₂ adsorption/desorption isotherms (a) and the corresponding pore-size distribution (b) of mSiO₂ samples.

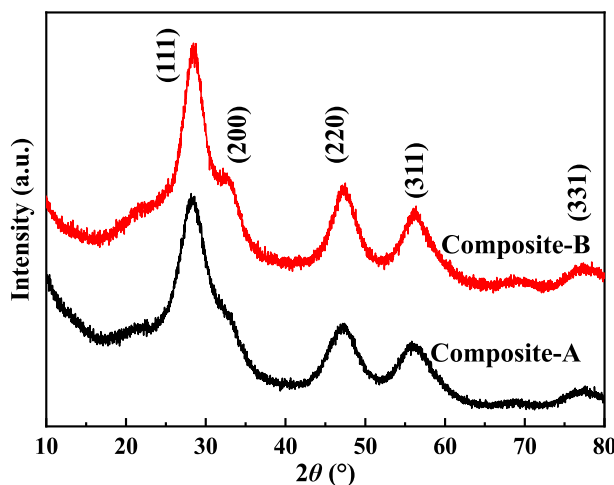


Fig. 5. Wide-angle XRD patterns of composite particles.

hysteresis loop is not obvious compared to typical mesoporous silica materials [20], which may be attributed to the coexistence of meso- and micro-pores for the obtained mSiO₂ spheres. The calculated BET surface area and pore volume is 1626.53 m²/g and 0.81 cm³/g, respectively. In addition, the pore-size distribution curve (Fig. 4b) derived from BJH model and the adsorption branch data reveals a narrow pore-size distribution with an average pore diameter of 2.76 nm.

The chemical composition and phase structure of the composites were examined by XRD analyses (Fig. 5). The peaks located at $2\theta = 28.5^\circ, 32.7^\circ, 47.4^\circ, 56.2^\circ$, and 77.4° can be indexed to the characteristic (111), (200), (220), (311), and (331) reflections of cubic fluorite-type

phase CeO₂ (PDF 34-0394) materials [21]. The typical diffraction peaks of Er₂O₃ cannot be detected from the XRD pattern of the Er³⁺-doped samples (composite-B), confirming the successful Er³⁺-doping in CeO₂ lattices and the formation of Ce-Er-O solid solutions. Ionic radius of Er³⁺ (0.089 nm) is slightly smaller than that of Ce⁴⁺ (0.097 nm), hence lattice contraction is expected due to incorporation of Er³⁺-doping in CeO₂ lattices. According to the Scherrer's equation and the (111) XRD diffractions, the lattice parameter of undoped CeO₂ (composite-A) and Er³⁺-doped CeO₂ (composite-B) were calculated to be ca. 0.541 nm and 0.536 nm, respectively. The slightly reduced lattice parameter may be attributed to the replacement of Ce⁴⁺ with smaller Er³⁺ (0.097 nm vs 0.089 nm). Moreover, the average crystallite size of undoped and Er³⁺-doped CeO₂ is ca. 5.2 nm and 5.4 nm, respectively.

Fig. 6 shows the typical FESEM images of the composite-A and composite-B samples. After coating, the resulting composites well maintain the initial spherical morphologies, and the outer surfaces are relatively rough compared to the bare mSiO₂ (Fig. 2a). The particle sizes of composite-A (Fig. 6a) and composite-B (Fig. 6b) were determined to be 249 ± 14 nm and 251 ± 16 nm, respectively. By comparison with the uncoated mSiO₂ cores (212 ± 8 nm), the CeO₂ shell thickness of the composite particles was estimated to be 15–20 nm.

Low-magnification TEM images of the composites (Fig. 7a and c) reveal that the mSiO₂ cores are fully coated by plenty of CeO₂ nanoparticles, confirming the core/shell structure formations for composite-A and composite-B. The corresponding high-resolution TEM images (Fig. 7b and d) clearly demonstrate the distinct lattice fringes of undoped CeO₂ (composite-A) and Er³⁺-doped CeO₂ (composite-B). And the interplanar distances of undoped and Er³⁺-doped CeO₂ are ca. 0.33 nm and 0.32 nm, respectively, which are assigned to the (111) plane of CeO₂ and consistent with the presented XRD results (Fig. 5).

To further identify the core/shell structure and elemental composition of composite samples, the HADDF-STEM (Fig. 8a) and the

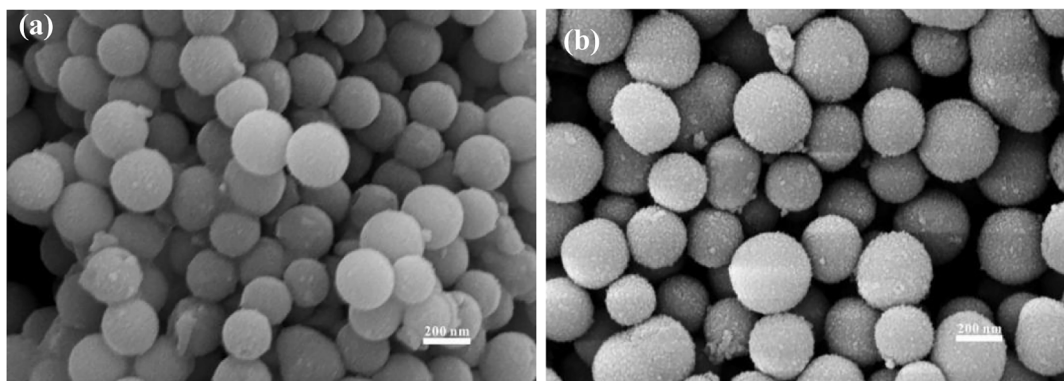


Fig. 6. FESEM images of (a) composite-A and (b) composite-B.

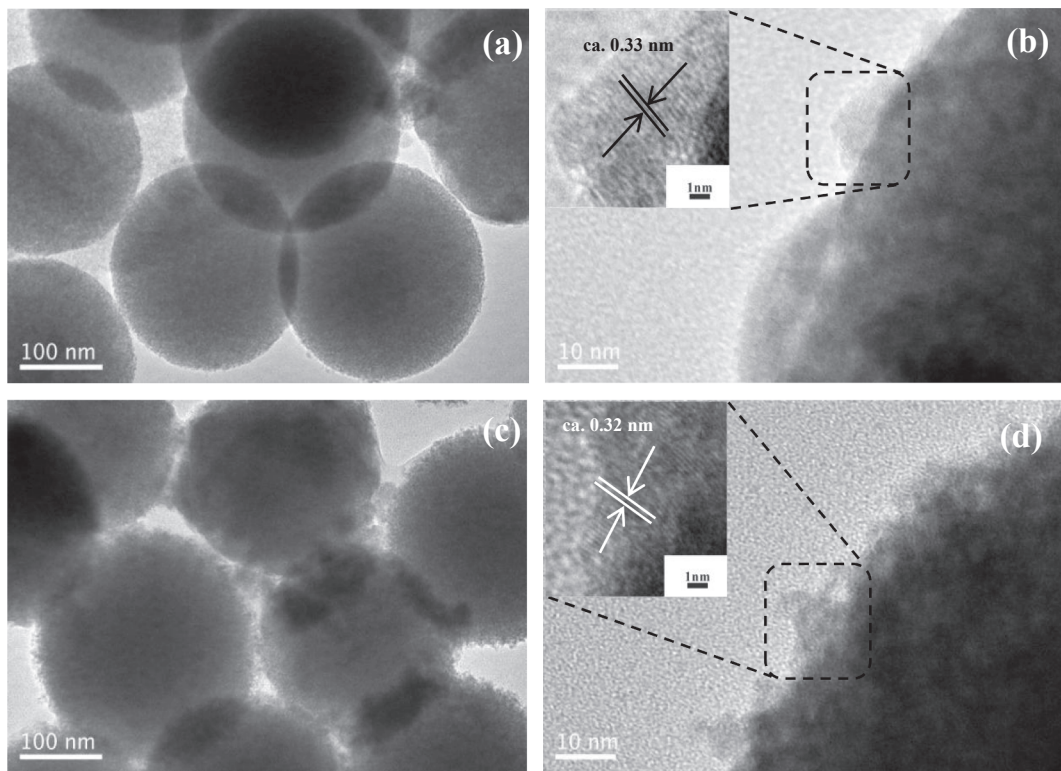


Fig. 7. Low-magnification and high-resolution TEM images of (a, b) composite-A and (c, d) composite-B.

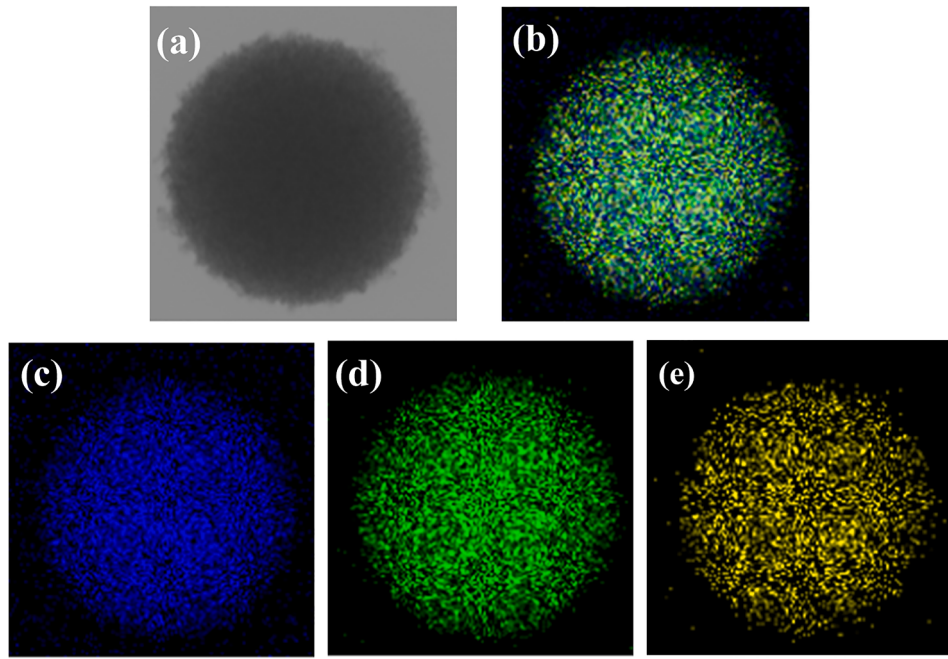


Fig. 8. HADDF-STEM image (a) and EDX elemental mapping: (b) Si-Ce-Er overlap, (c) Si, (d) Ce, (e) Er of composite-B.

corresponding EDX elemental mapping (Fig. 8b-e) analyses were performed on an individual composite-B particle. As revealed by the Ce-Er-Si elemental overlap, the Si atoms are mostly located in the internal area of the individual particle, while the Ce and Er atoms are uniformly distributed throughout the nanostructure. These provided results further confirm the formation of the well-defined core/shell structure for composite-B samples, which possess silica cores and Er^{3+} -doped ceria shells.

UV-Vis spectra of composites (Fig. 9a) present an intensive absorption peak at ca. 340 nm, which may be attributed to the electronic transition from O 2p to Ce 4f level. To obtain the band gap energy (E_g) of the composites, Schuster-Kubelka-Munk absorption functions ($\alpha h\nu$) were plotted against the photon energy ($h\nu$) according to the Eq. (2):

$$(\alpha h\nu)^{1/n} = A(h\nu - E_g) \quad (2)$$

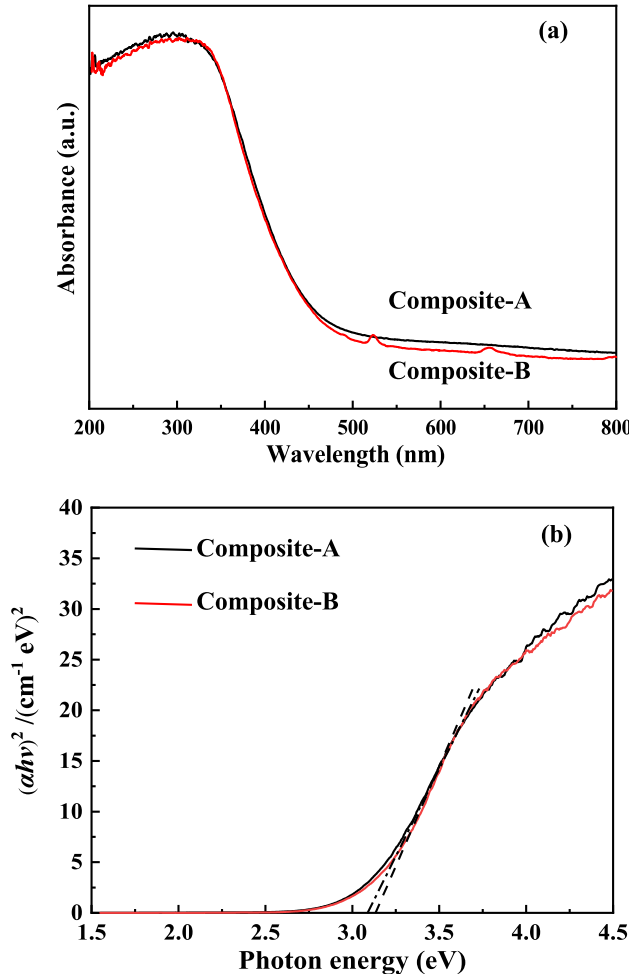


Fig. 9. UV–vis absorption spectra (a) and Schuster-Kubelka-Munk functions (b) of binary particles.

where α is the absorption coefficient, h is the Planck's constant, ν is the frequency of vibration, $h\nu$ is the photon energy, A is the proportionality constant, and the value of n depends on the type of optical transition of the semiconductor ($n = 2$ for indirect transition). As shown in Fig. 9b, the approximated band gap can be determined from the straight-line x -intercept. The E_g values for composite-A and composite-B were determined to be 3.15 eV and 3.10 eV, respectively. In addition, the conduction band potential (E_{CB}) and valence band potential (E_{VB}) can be calculated by the following Eqs. (3), (4) using the determined E_g .

$$E_{VB} = \chi - E_c + 1/2E_g \quad (3)$$

$$E_{CB} = E_{VB} - E_g \quad (4)$$

where χ is the absolute electronegativity of the semiconductor (χ is 5.57 eV for CeO_2) [22], E_c is the energy of free electrons on the hydrogen scale (4.5 eV), and E_g is the optical band gap. The calculated E_{CB} and E_{VB} potentials of composite-A are -0.50 and 2.65 eV, respectively. And the E_{CB} and E_{VB} values for composite-B are -0.48 and 2.62 eV, respectively. Er^{3+} -doping in CeO_2 lattice contribute to the E_g reduction for composite-B with respect to undoped composite-A. It may be attributed to the ground and excited states in the mid band gap of CeO_2 created by Er^{3+} -doping [23]. These energy states of Er^{3+} take up many of the excited electrons originating from O 2p level [24]. The substitution of Ce^{4+} with Er^{3+} may also increase the oxygen vacancy and Ce^{3+} concentrations of CeO_2 materials due to a charge compensation mechanism, which leads to the formation of localized states within the band gap. It also

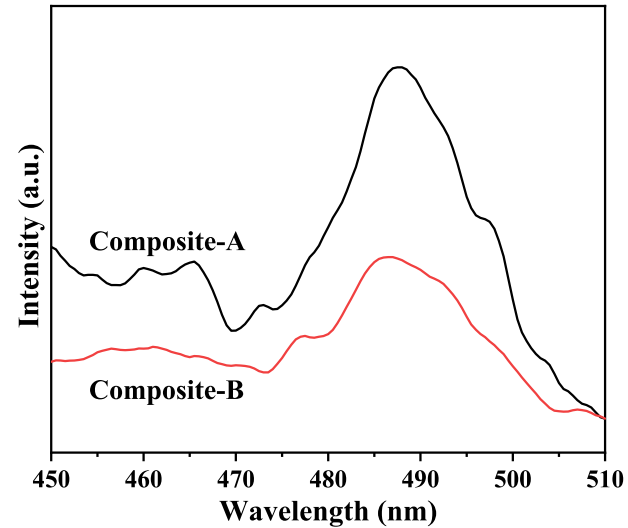


Fig. 10. PL spectra of composite samples.

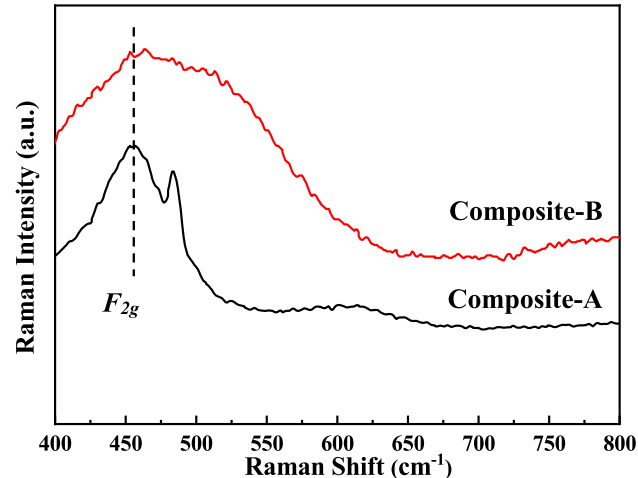


Fig. 11. Raman spectra of composite samples.

contributes to effective reduction in band gap and effective separation of electron-hole pair. In this work, the improved photocatalytic activity of Er^{3+} -doped CeO_2 may accelerate the soft layer formation at the surfaces, and achieve an enhanced MRR during PCMP with composite-A abrasives.

PL observations (Fig. 10) were employed to track the chance of electron-hole pair recombination in materials. Since the intensity of PL emission spectra is related to the recombination of the excited electrons and holes, it commonly recognized that a decreased PL intensity suggest a reduced recombination rate of electron-hole pairs under light irradiation [25]. By comparison with composite-A, the composite-B present a relatively low room-temperature PL intensity, verifying an improved efficient separation of electron-hole pair and an enhanced photocatalytic activity (consistent with UV–vis results) [26]. Moreover, the peaks located at ca. 487 nm may also be attributed to oxygen vacancies in ceria.

Raman spectra (Fig. 11) of the binary composites include the main band peak at ca. 460 cm^{-1} , corresponding to the Raman vibration mode (F_{2g}) of the cubic fluorite-type CeO_2 lattices. Moreover, the spectra corresponding to composite-B do not present the typical Er_2O_3 band, confirming the Er^{3+} -doping in CeO_2 lattices and the formation of Ce-Er-O solid solutions [27,28]. The presence of Er^{3+} in CeO_2 lattices can deform the structures, resulting in a reduced fluorite-characteristic peak

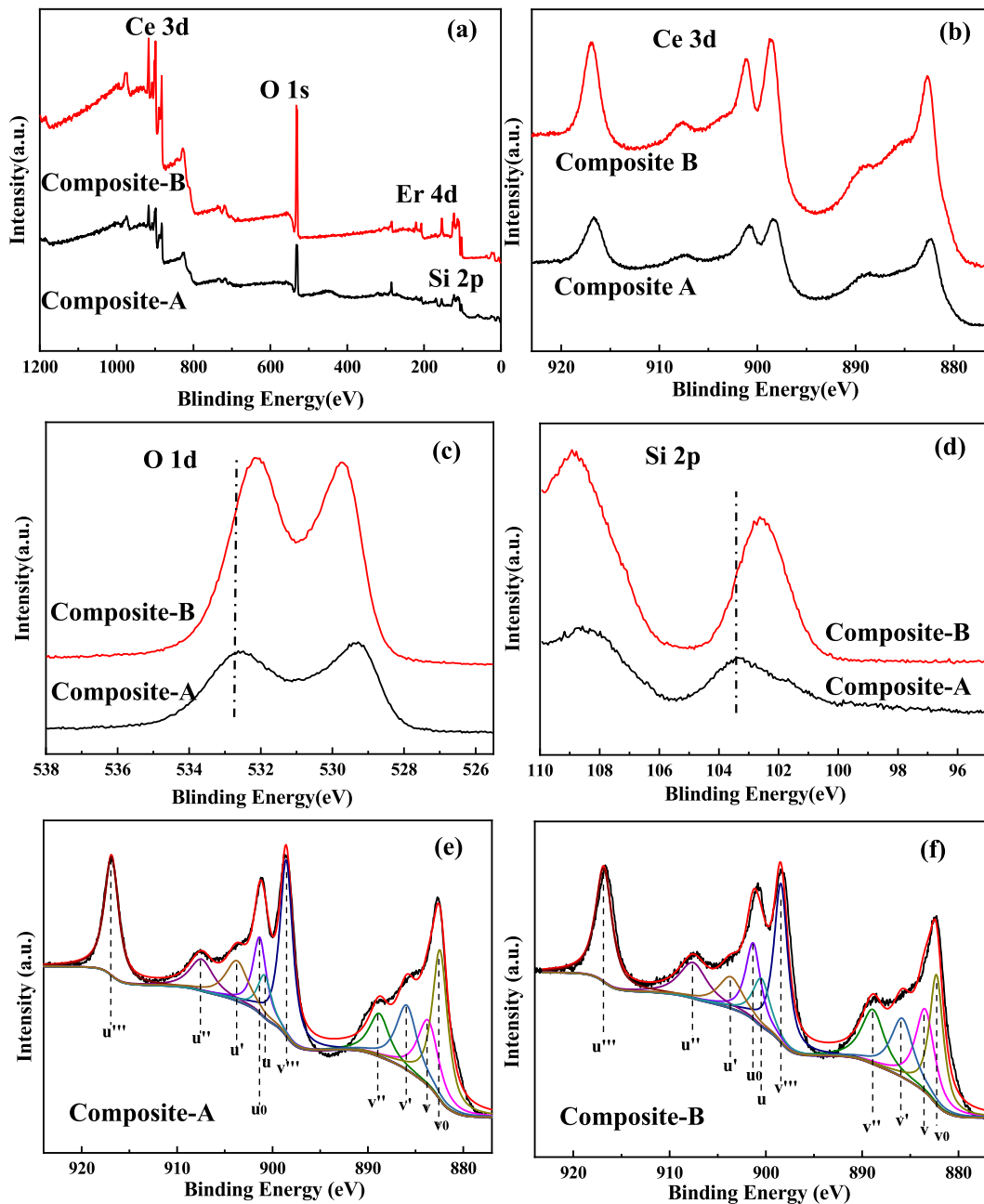


Fig. 12. XPS survey spectra (a), Ce 3d (b), O1s (c), Si 2p (d), and Ce 3d core level spectra (e, f) of composite particles.

intensity for the Er^{3+} -doped composite-B. Raman spectra complement the XRD results very well and detect the changes in the vibrational structure of CeO_2 caused by the incorporation of Er^{3+} .

In addition, the Raman peaks at ca. 620 cm^{-1} can be attributed to the oxygen vacancies resulting from the presence of Ce^{3+} in CeO_2 lattices or the defects caused by small size effects [29]. The peak intensity of the band at 460 cm^{-1} and 620 cm^{-1} is denoted as I_{460} and I_{620} , respectively. It is commonly recognized that the ratio of I_{620}/I_{460} reflects the concentration of oxygen vacancies in CeO_2 materials [30]. The calculated I_{620}/I_{460} for composite-B (ca. 0.43) is higher than that of composite-A (ca. 0.33), suggesting increased oxygen vacancies after Er^{3+} -doping in CeO_2 lattices. It may be resulted from the reduced oxygen vacancy (V_O) formation energy of CeO_2 materials by rare earth elements-doping. Ke and coworkers [29] calculated the V_O formation energy (E_V) at the nearest-neighbor site and the next nearest-neighbor site to the surface dopant via density functional theory (DFT) using the equation (5):

$$E_V = E(\text{CeO}_2 \text{ with } V_O) + 1/2E(O_2) - E(\text{CeO}_2) \quad (5)$$

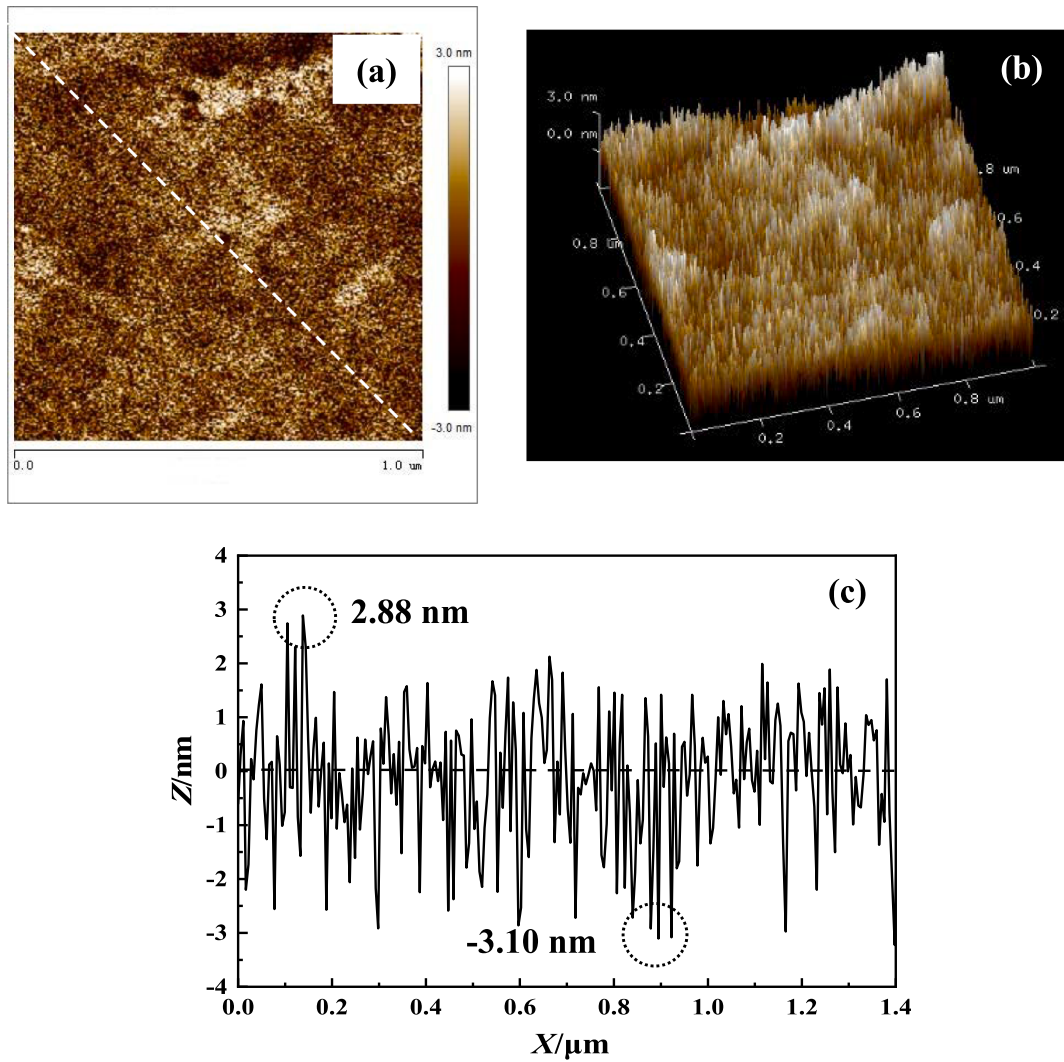
where E_V is the oxygen vacancy (V_O) formation energy, $E(\text{CeO}_2 \text{ with } V_O)$ and $E(\text{CeO}_2)$ are the total energies of the optimized CeO_2 with and without one oxygen vacancy, and $E(O_2)$ is the total energy for the ground state of an optimized O_2 molecule in the gas phase. It was found that the E_V (0.21–0.39 eV) for all the lanthanides (La^{3+} , Nd^{3+} , Gd^{3+} , Ho^{3+} , Lu^{3+})-doped ceria was lower than that for undoped one (1.54 eV). In photochemical and/or photophysical applications, oxygen vacancies contribute to the effective separation of photo-generated carriers from recombination, and the photo-induced h^+ further oxidize $\text{OH}^-/\text{H}_2\text{O}$ into $\cdot\text{OH}$ [27,28,31].

The elements Ce, O, and Si (Ce 3d, O 1s, and Si 2p binding energies) can be detected from the wide-scan XPS spectra (Fig. 12a) of the obtained composites. And the peak at ca. 167.7 eV is attributed to the binding energy of Er 4d [17,18], also revealing the successful Er^{3+} -

Table 1

Oxidation states and binding energies of the Ce species for composite samples.

	v_0 (Composite A/B)	v (Composite A/B)	v' (Composite A/B)	v'' (Composite A/B)	v''' (Composite A/B)
Ce3d _{5/2} Oxidation state (v)	Ce ³⁺	Ce ⁴⁺	Ce ³⁺	Ce ⁴⁺	Ce ⁴⁺
BE (eV)	883.3/881.1	884.3/882.6	885.8/884.9	889.7/888.2	899.6/898.7
Area (%)	5.9/3.9	7.6/3.5	4.7/2.8	6.5/2.7	6.7/4.8
	u (Composite A/B)	u_0 (Composite A/B)	u' (Composite A/B)	u'' (Composite A/B)	u''' (Composite A/B)
Ce3d _{3/2} Oxidation state (v)	Ce ³⁺	Ce ⁴⁺	Ce ³⁺	Ce ⁴⁺	Ce ⁴⁺
BE (eV)	900.7/900.2	902.1/901.1	903.3/902.7	908.6/907.4	917.9/916.6
Area (%)	4.8/1.8	5.7/2.5	3.5/1.7	4.8/2.2	9.2/4.1

**Fig. 13.** 2D-AFM image (a), 3D-AFM image (b) and line-scan profile (c) of the original surface.

doping in CeO₂ lattices. As shown in Fig. 12b, the XPS Ce 3d multiplex reveal the presence of Ce³⁺ and Ce⁴⁺ ions in composites. The peaks centered at ca. 901.8 eV and 882.9 eV can be attributed to the Ce³⁺ contributions, and the peaks located at ca. 917.2 eV and 899.0 eV can be attributed to the Ce⁴⁺ contributions. In addition, the chemical shifts of O 1s (Fig. 12c) and Si 2p (Fig. 12d) can be tracked for the composites before and after Er³⁺-doping. It is commonly recognized that there always coexist with a small amount of Ce³⁺ at the surfaces of CeO₂. Fig. 12e (composite-A) and f (composite-B) show the Ce 3d electron core

level XPS spectra and the changes in Ce 3d_{3/2} and Ce 3d_{5/2} components depending on the Ce³⁺ and Ce⁴⁺ oxidation states. The v_0 , v' , u and u' peaks are the characteristic peaks of Ce³⁺ ions, and the v , v'' , v''' , u_0 , u'' and u''' are ascribed to Ce⁴⁺ ions. The peaks of Ce³⁺ and Ce⁴⁺ ions were identified by nonlinear Gaussian peak fittings method after elimination of the backgrounds. The concentration of Ce³⁺ was calculated according to the Eq. (6) using a semiquantitative analysis of the integrated peak area:

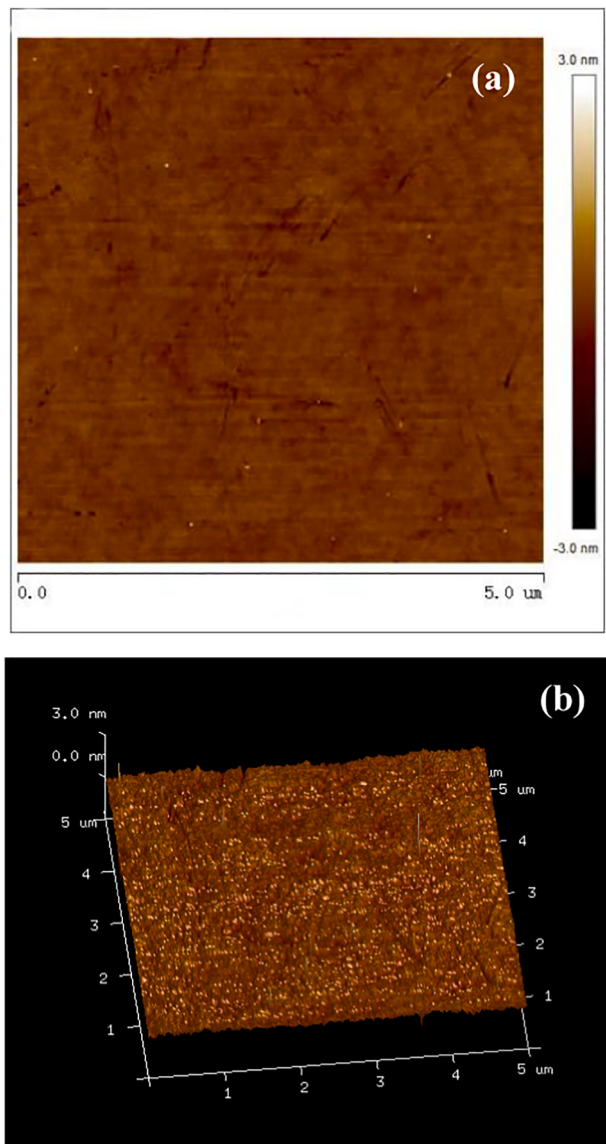


Fig. 14. 2D-AFM image (a) and 3D-AFM image (b) of the surface polished with rigid composites with solid silica cores.

$$[Ce^{3+}] = \frac{S_{v_0} + S_{v'} + S_u + S_{u'}}{S_{v_0} + S_v + S_{v'} + S_{v''} + S_{v'''} + S_{u_0} + S_u + S_{u'} + S_{u''} + S_{u'''}} \quad (6)$$

where S_i is the integrated area corresponding to peak “ i ”. The data corresponding to the oxidation states, the binding energies, and the areas of Ce species are provided in Table 1. The Ce^{3+} ratios for composite-A and composite-B were calculated to be 31.8% and 34.4%, respectively. It was confirmed that Er^{3+} -doping treatment resulted in an increased Ce^{3+} content in the coated CeO_2 nanoparticles for composite-B. In addition, the Ce^{3+} in CeO_2 materials are related to the amount and active of oxygen vacancies, suggesting an enhanced photocatalytic activity for the composite-B. In CMP and PCMP, Ce^{3+} at the surfaces of CeO_2 abrasives may act as active sites and facilitate the tribochemical reactions between silica and ceria [32], and contribute to an enhanced MRR towards silica.

3.2. Polishing performance and mechanism of composite abrasives

3.2.1. Surface characteristics

Two-dimensional (2D)-, 3D-AFM images, and cross-sectional profile curves of the surfaces before and after CMP/PCMP with different

abrasives were examined in terms of high-resolution AFM. The 2D-AFM image of original substrate present uneven morphologies (Fig. 13a) with root-mean-square (RMS) roughness of 0.8–1.0 nm. A large number of nano-asperities can also be clearly observed from the corresponding 3D-AFM image (Fig. 13b). Topographical variations were further explored in terms of the cross-sectional line trace along a diagonal line in 2D-AFM image. As shown in Fig. 13c, the maximum asperity height and the maximum valley depth in the profile curve were determined to be 2.88 nm and 3.10 nm, respectively. After CMP with rigid composite abrasives with solid silica cores and ceria shells, a certain number of micro-scratches can also be clearly tracked from the AFM analyses (Fig. 14).

The type, structure, and property of abrasives play a key role in determining the final surface quality and MRR. Compared to traditional rigid ceria abrasives, the hybrid abrasives containing polymer or mSiO₂ elastic cores and ceria active shells [8–12,33,34] contributed to mechanical damage elimination and surface quality improvement. Fig. 15 shows the typical 2D-AFM images of the substrate surfaces after conventional CMP (without UV irradiation) and PCMP (with UV irradiation) using composite-A and composite-B abrasives. The uniform colors in AFM-height images commonly suggest superior surface quality and flatness. In both CMP and PCMP applications, the as-obtained composite abrasives achieve flat and smooth surfaces without obvious scratching grooves, etching pits and residual nanoparticles. As confirmed by AFM analyses, the composite-A abrasives under conventional CMP conditions achieve the ultra-smooth surface with an RMS roughness of 0.18 ± 0.01 nm. In PCMP conditions, the composite-A and composite-B abrasives allow a comparable RMS surface roughness of 0.17 ± 0.01 nm and 0.16 ± 0.01 nm, respectively. The surface finishes at an atomic-scale of less than 0.2 nm can be achieved using the binary particles as functionalized abrasives in both CMP and PCMP experiments.

RMS surface roughness is the average of the measured height deviations taken within the evaluation length and measured from the mean line, and the statistical measure of roughness is commonly used to compare surfaces. It is worth noting that the calculated RMS values may be misleading because they cannot provide information about the spatial or textural variations in the profile [34]. An improved surface planarization degree can be confirmed by reduced topographical variations. The profile curves along the diagonal lines in the corresponding 2D-AFM images (Fig. 15) were further tracked. For the surface achieved by composite-A under CMP conditions, the line trace (Fig. 16a) indicate the maximum asperity height of 0.52 nm and the maximum valley depth of 0.45 nm. In PCMP applications (Fig. 16b and c), the maximum asperity height reduces from 2.88 nm to 0.38 nm (composite-A) and 0.35 nm (composite-B), and the maximum valley depth decreases from 3.10 nm to 0.39 nm (composite-A) and 0.36 nm (composite-B). Although the surfaces exhibit a comparable RMS roughness after CMP and PCMP tests, the cross-sectional analyses confirm that the PCMP conditions (with UV irradiation) further contribute to the topographical variation reductions. By comparison with the initial surface (Fig. 13b), the corresponding 3D-AFM images (Fig. 17) derived from the 2D-AFM images using NanoScope software clearly reveal and confirm the difference and removal of the nano-asperities at the polished surfaces using the developed meso-silica/ceria binary abrasives.

Recently, Gao and coworkers [11] reported the ECMP performance of the PS/ CeO_2 core/shell abrasives with different shell thicknesses. The effects of shell thickness on the contact areas between abrasives and surfaces, and on the indentation depth of an abrasive into a surface were also explored on the basis of the contact-area and the indentation-depth theories. It was proposed that the non-rigid PS/ CeO_2 ($E: 6.4\text{--}14.3$ GPa) achieved an enlarged contact area and reduced contact stress between the particle and the surface compared to rigid CeO_2 ($E: 264.1$ GPa). As a result, the PS/ CeO_2 abrasives contributed to indentation depth and surface roughness reductions. In our previous work [35], the compressive E of the mSiO₂ spheres (ca. 316 nm in particle size and 2.5 nm in pore size) were fitted and calculated by analyzing the AFM force-displacement curves on the basis of the Hertzian contact model. The

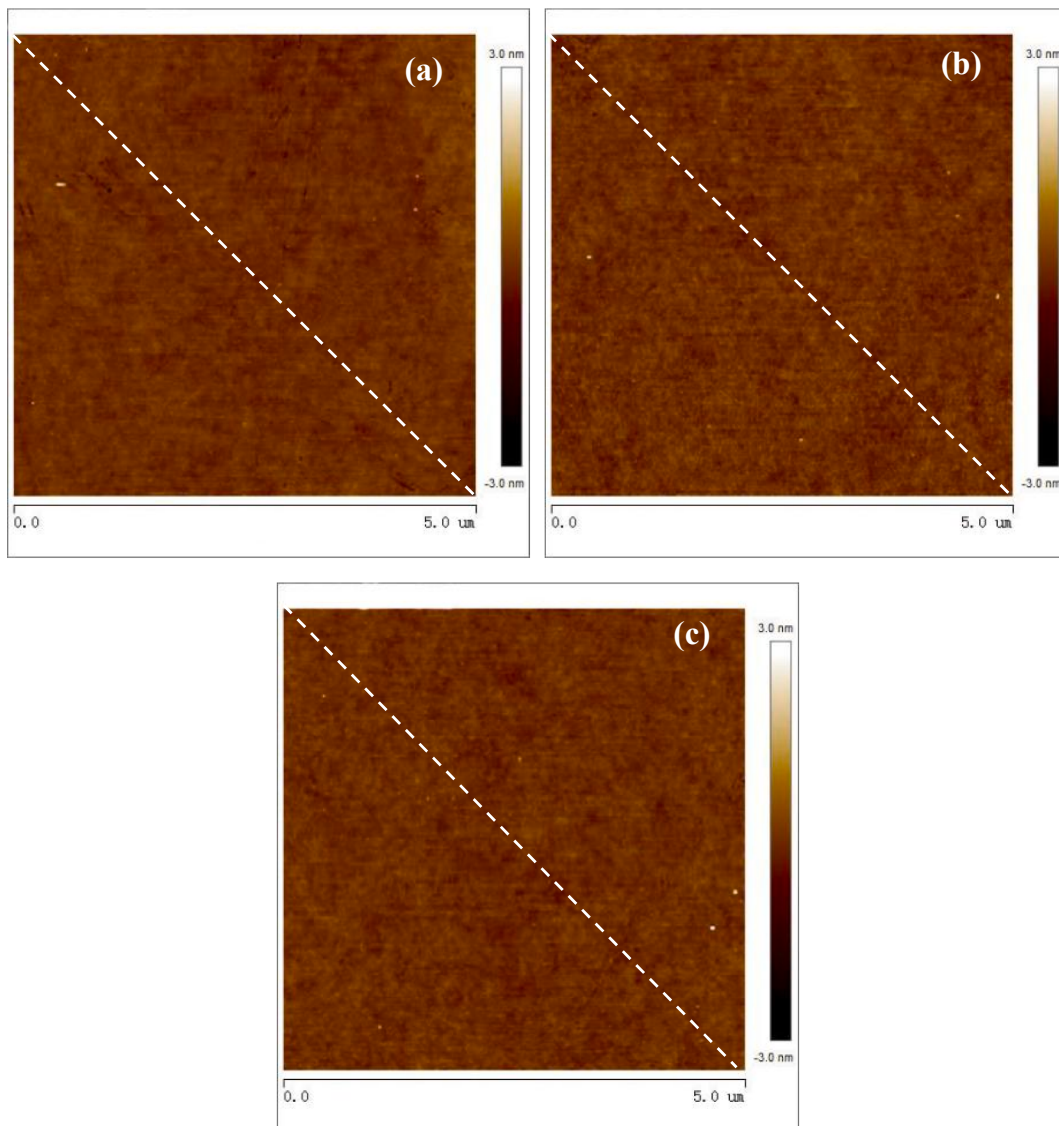


Fig. 15. 2D-AFM images of the surfaces after (a) CMP with composite-A, (b) PCMP with composite-A, and (c) PCMP with composite-B.

average E of mSiO₂ was determined to be 5.30 GPa, which were much lower than that of solid dense silica particles (ca. 72 GPa).

The presented results clearly indicate that the meso-silica/ceria binary abrasives contribute to surface roughness and topographical variation reductions. As reported in the literatures [11,36,37], the elastic response and E of core/shell composite particles are mainly determined by the mechanical property and the shell thickness of their core materials. In this work, the proposed particles may also behave reduced overall compressive E and non-grid mechanical properties, originating from the presence of low-modulus mSiO₂ cores. The spring-like composites might be deformed when stressed, leading to increased contact areas between abrasives and surfaces. Moreover, a gentle and uniform material removal with low mechanical damages might occurred during CMP and PCMP processes, resulting from the well adaption of pad asperities and abrasive particles. Therefore, the composite abrasives with mSiO₂ cores achieved an improved surface quality compared to the rigid abrasives with solid silica ones.

3.2.2. Polishing efficiency

The surface characteristics and material removal rates for CMP and PCMP experiments achieved by composite-A and composite-B are presented in Table 2. Compared to the CMP (without UV irradiation), the

average MRR of composite-A abrasives under PCMP (with UV irradiation) is increased by 74%, from 38 ± 13 nm/min to 66 ± 19 nm/min. The MRR is further enhanced by 50% for the Er³⁺-doped composite-B under PCMP, which achieves an average MRR of 99 ± 18 nm/min. It can be concluded that both UV irradiation and Er³⁺-doping contributes to the MRR enhancements for the meso-silica/ceria binary abrasives.

It is commonly recognized that the formation of ultra-smooth surfaces involves mechanical abrasion removals and chemical corrosion modifications in CMP/PCMP. The substrate surfaces are firstly softened by chemical corrosion or oxidation, and subsequently removed by mechanical friction and abrasion. Several mathematical models [38,39] over silica materials confirmed that an enhanced oxidative activity of polishing slurries contributed to the formation of chemically modified layer and resulted in an increased MRR . Therefore, an improved surface quality combined with an enhanced MRR may result from the proper and dynamical balancing between the mechanical action and the chemical action in material removal processes.

The enhanced MRR after Er³⁺-doping and UV irradiation treatments for the developed abrasives may be attributed to the combined effect of following factors. Based on the electron transfer mechanism of conventional photocatalytic processes, when the light energy is higher than the E_g of photocatalyst materials, the h^+ are generated in the valence

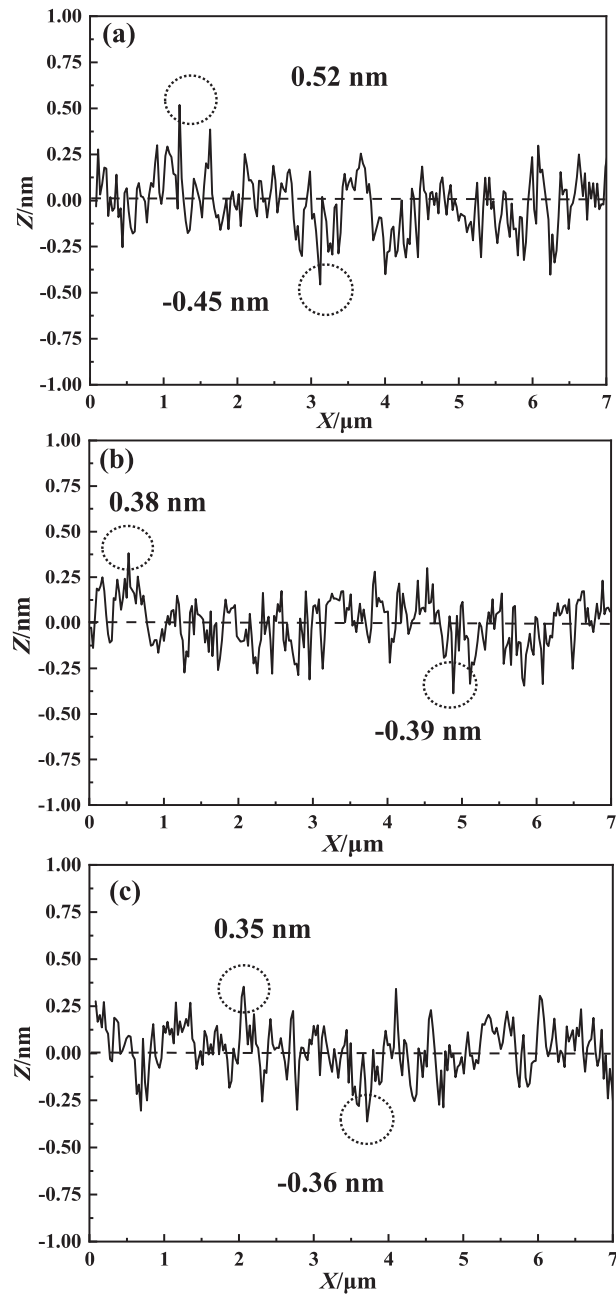


Fig. 16. Line-scan profiles of the surfaces after (a) CMP with composite-A, (b) PCMP with composite-A, and (c) PCMP with composite-B.

band. Then, the photogenerated electron e^- of the VB will be excited and move to CB, and the $\text{OH}^-/\text{H}_2\text{O}$ will be oxidized into the $\cdot\text{OH}$ by the photo-induced h^+ . In this work, the provided UV-vis, Raman, and PL results suggest an improved photocatalytic activity of the Er^{3+} -doped CeO_2 in composite-B. It can be explained by effective reduction in E_g due to the creation of ground and excited states in the mid band gap, which leads to the formation of localized states and takes up many of the excited electrons coming from O 2p level [23,40]. The substitution of Ce^{4+} with Er^{3+} may result in an increased concentration of the active sites (oxygen vacancy and Ce^{3+}) due to a charge compensation mechanism. Highly reactive photoinduced holes are produced on the surfaces of the Er^{3+} -doped composites, and more $\cdot\text{OH}$ are generated in polishing slurries. Therefore, Er^{3+} -doping treatment facilitates the efficient separation of photogenerated carriers, and the photo-induced h^+ will oxidize $\text{OH}^-/\text{H}_2\text{O}$ into the $\cdot\text{OH}$ with a strong oxidation capability. In this work, the enhanced chemical modification and/or corrosion activities can

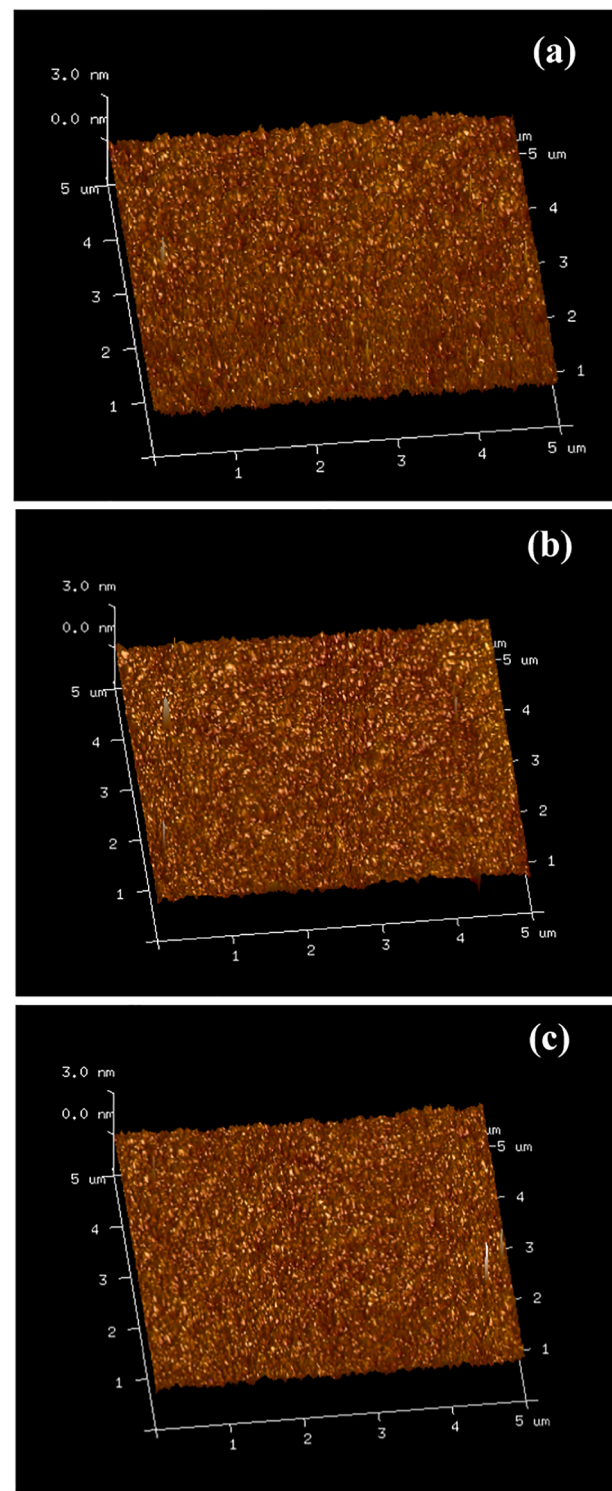


Fig. 17. 3D-AFM images of the surfaces after (a) CMP with composite-A, (b) PCMP with composite-A, and (c) PCMP with composite-B.

accelerate the formation of the reacted soft layers and finally contribute to the MRR improvement in PCMP experiments.

CeO_2 -based particles are one of the most effective abrasives towards silica materials due to their tribochemical reaction activity and chemical tooth effect (the formation and breakage of the $\text{Ce}-\text{O}-\text{Si}$ bond) proposed by Cook [13]. In alkaline conditions, the dissolved silica is adsorbed onto the CeO_2 abrasive surfaces or released into slurries. And the reacted products are removed by the tribochemical reaction and/or

Table 2
Surface characteristics and MRR data for CMP and PCMP experiments.

Samples	Composite-A		Composite-B	
	CMP	PCMP	CMP	PCMP
RMR roughness (nm)	0.18 ± 0.01	/	0.17 ± 0.01	0.16 ± 0.01
Maximum asperity height (nm)	0.52	/	0.38	0.35
Maximum valley depth (nm)	0.45	/	0.39	0.36
MRR (nm/min)	38 ± 13	66 ± 19	71 ± 23	99 ± 18

the mechanical abrasion between abrasives and surfaces. Moreover, the Ce³⁺ in CeO₂ surfaces contribute to the Ce—O—Si bonding and the hydration layer formations [32,33]. In this work, XPS analyses confirm that Er³⁺-doping treatment contribute to an increased Ce³⁺ concentration in the CeO₂ surfaces of composite-B. The improved tribochemical activity of CeO₂ is expected to accelerate the Ce—O—Si bonding and the hydration layer formations. It is also beneficial to the MRR enhancement in PCMP processes.

In summary, we focus on the controlled design and fabrication of core/shell structured meso-silica/ceria binary particles as novel abrasives for improved PCMP performance. The presented data clearly reveal that Er³⁺-doping and UV irradiation treatments for the functionalized abrasives contribute to the surface roughness and topographical variation reductions, as well as the MRR enhancement. However, the actual role of the functionalized binary abrasives in PCMP is still ambiguous. For the non-rigid abrasive particles, the adhesion force might dominate the interfacial contact while the elastic deformation occurred. And the removal of the reacted atoms might be derived from the dynamic formation and breakage of the interfacial adhesion bonds by mechanical actions. The in-depth investigations about the material removal mechanism of the functionalized meso-silica/ceria binary abrasives will be performed in our next work.

4. Conclusions

The worm-like meso-silica (mSiO₂) spheres with a particle size of ca. 200 nm, a specific area of 1626.5 m²/g, and a pore size of 2.76 nm were prepared via a modified Stöber approach. Well-defined core/shell structured mSiO₂/CeO₂ (composite-A) and mSiO₂/Ce_{0.83}Er_{0.17}O₂ (composite-B) binary particles were further synthesized via a chemical precipitation method. The as-prepared materials were characterized by XRD, FESEM, HRTEM, HADDF-STEM, EDX mapping, UV-vis, Raman, XPS, PL, and N₂ adsorption–desorption measurements. Er³⁺-doping in CeO₂ nanocrystallines presented a reduced band gap, and an enhanced separation efficiency of electron-hole pair and concentration of oxygen vacancy, suggesting an improved photocatalytic activity. In addition, Er³⁺-doping treatment contributed to an increased Ce³⁺ content (34.4% vs 31.8%) and an improved tribochemical activity for the grafted CeO₂ nanoparticles. In both CMP and PCMP experiments, the functionalized composite abrasives achieved ultra-smooth and damage-free surfaces with an atomic-scale roughness of less than 0.2 nm, possibly resulting from their low-modulus mSiO₂ cores. Er³⁺-doping and UV irradiation treatments towards the binary abrasives contributed to the topographical variation reduction and MRR enhancement. It might be attributed to the improved photocatalytic activity and tribochemical activity, as well as the proper and dynamical balance between the formation and removal of the chemically reacted layers. The proposed meso-silica/ceria binary composite particles can be promising abrasives for achieving high-quality and high-efficiency polishing and is expected to be available in many other applications. The structure optimization and performance control over the functionalized meso-silica/ceria binary abrasives for mechanical, tribochemical, and photocatalytic properties are under in-depth investigations in our group. The results of this

investigation will encourage the researchers to develop and design other functionalized composite abrasives for PCMP (or ECMP) applications.

CRediT authorship contribution statement

Ailian Chen: Conceptualization, Methodology, Formal analysis, Investigation, Data curation, Writing - original draft, Visualization. **Yuhan Duan:** Validation, Visualization, Software. **Zhaoyu Mu:** Methodology, Investigation. **Wenjie Cai:** Methodology, Formal analysis. **Yang Chen:** Conceptualization, Resources, Writing - review & editing, Supervision, Project administration, Funding acquisition.

Declaration of Competing Interest

The authors declare that they have no known competing financial interests or personal relationships that could have appeared to influence the work reported in this paper.

Acknowledgements

The paper is supported financially by National Natural Science Foundation of China (Grant Nos. 51575058 and 51875052), and the Priority Academic Program Development of Jiangsu Higher Education Institutions (PAPD).

References

- [1] J. Wang, T.Q. Wang, G.S. Pan, X.C. Lu, Effect of photocatalytic oxidation technology on GaN CMP, *Appl. Surf. Sci.* 361 (2016) 18–24.
- [2] J. Wang, T.Q. Wang, G.S. Pan, X.C. Lu, Effects of catalyst concentration and ultraviolet intensity on chemical mechanical polishing of GaN, *Appl. Surf. Sci.* 378 (2016) 130–135.
- [3] Z. Yuan, Y. He, X. Sun, Q. Wen, UV-TiO₂ photocatalysis assisted chemical mechanical polishing 4H-SiC wafer, *Mater. Process.* 33 (2018) 1214–1222.
- [4] Q.S. Yan, X. Wang, Q. Xiong, J.B. Lu, B.T. Liao, The influences of technological parameters on the rate of ultraviolet photocatalytic reaction and photocatalysis-assisted polishing effect for SiC, *J. Cryst. Growth* 531 (2020) 125379.
- [5] X. Yu, B. Zhang, R. Wang, Z. Kao, S. Yang, W. Wei, Effect of photocatalysts on electrochemical properties and chemical mechanical polishing rate of GaN, *Mat. Sci. Semicon. Proc.* 121 (2021) 105387.
- [6] Z.W. Zhong, Recent developments and applications of chemical mechanical polishing, *Int. J. Adv. Manuf. Tech.* 109 (2020) 1419–1430.
- [7] F. Meng, Z. Zhang, P. Gao, T. Liu, Y. Boyjoo, D. Guo, Design of composite abrasives and substrate materials for chemical mechanical polishing applications, *Appl. Nanosci.* 10 (2020) 1379–1393.
- [8] Y. Chen, R.W. Long, Polishing behavior of PS/CeO₂ hybrid microspheres with controlled shell thickness on silicon dioxide CMP, *Appl. Surf. Sci.* 257 (2011) 8679–8685.
- [9] J. Murata, Y. Ueno, K. Yodogawa, T. Sugiura, Polymer/CeO₂-Fe₃O₄ multicomponent core-shell particles for high-efficiency magnetic-field-assisted polishing processes, *Int. J. Mach. Tool Manu.* 101 (2016) 28–34.
- [10] J. Murata, K. Yodogawa, K. Ban, Polishing-pad-free electrochemical mechanical polishing of single-crystalline SiC surfaces using polyurethane-CeO₂ core-shell particles, *Int. J. Mach. Tool Manu.* 114 (2017) 1–7.
- [11] B. Gao, W.J. Zhai, Q. Zhai, Y.Q. Shi, Polystyrene/CeO₂ core/shell abrasives for high-quality 4H-SiC surface in ECMP: The effects of shell thickness, *ECS J. Solid State Sci.* 9 (2020) 044005.
- [12] B. Gao, W.J. Zhai, Q. Zhai, M.Z. Zhang, Novel polystyrene/CeO₂-TiO₂ multicomponent core/shell abrasives for high-efficiency and high-quality photocatalytic-assisted chemical mechanical polishing of reaction-bonded silicon carbide, *Appl. Surf. Sci.* 484 (2019) 534–541.
- [13] L.M. Cook, Chemical processes in glass polishing, *J. Non-Cryst. Solid* 120 (1990) 152–171.
- [14] M. Krishnan, J.W. Nalaskowski, L.M. Cook, Chemical mechanical planarization: Slurry chemistry, materials, and mechanisms, *Chem. Rev.* 110 (2010) 178–204.
- [15] H. Abdo, N. Keerthiraj, Q.A. Drmosh, D. Ponnamma, J. Wang, S. Prasad, M. Ahamed, C. Cheng, K. Byrappa, CeO₂ nanostructures enriched with oxygen vacancies for photocatalytic CO₂ reduction, *ACS Appl. Nano. Mater.* 3 (2020) 138–148.
- [16] M.A. Mavuso, P.R. Makgwane, S.S. Ray, Heterostructured CeO₂-M (M = Co, Cu, Mn, Fe, Ni) oxide nanocatalysts for the visible-light photooxidation of pinene to aroma oxygenates, *ACS Omega* 5 (2020) 9775–9788.
- [17] G. Han, M. Wang, D. Li, J. Bai, G. Diao, Novel upconversion Er, Yb-CeO₂ hollow spheres as scattering layer materials for efficient dye-sensitized solar cells, *Sol. Energ. Mater. Sol. C* 160 (2017) 54–59.
- [18] S. Chahal, A. Kumar, P. Kumar, Erbium-doped oxygen deficient cerium oxide: bi-functional material in the field of spintronics and photocatalysis, *Appl. Nanosci.* 10 (2020) 1721–1733.

- [19] Y. Chen, Z.F. Li, J.W. Qin, A.L. Chen, Monodispersed mesoporous silica (mSiO_2) spheres as abrasives for improved chemical mechanical planarization performance, *J. Mater. Sci.* 51 (2016) 5811–5822.
- [20] Y.L. Dai, V.P. Kumar, C. Zhu, M.J. MacLachlan, K.J. Smith, M.O. Wolf, Y. Dai, K. Pavan, C. Zhu, Mesoporous silica-supported nanostructured PdO/CeO_2 catalysts for low-temperature methane oxidation, *ACS Appl. Mater. Inter.* 10 (2017) 477–487.
- [21] Y.C. Huang, S.H. Wu, C.H. Hsiao, A.T. Lee, M.H. Huang, Mild synthesis of size-tunable CeO_2 octahedra for band gap variation, *Chem. Mater.* 32 (2020) 2631–2638.
- [22] Z.M. Yang, G.F. Huang, W.Q. Huang, J.M. Wei, X.G. Yan, Y.Y. Liu, C. Jiao, Z. Wan, A.L. Pan, Novel $\text{Ag}_3\text{PO}_4/\text{CeO}_2$ composite with high efficiency and stability for photocatalytic applications, *J. Mater. Chem. A* 2 (2013) 1750–1756.
- [23] K.S. Ranjith, P. Saravanan, S.H. Chen, C.L. Dong, C.L. Chen, S.Y. Chen, K. Asokan, R.T.R. Kumar, Enhanced room-temperature ferromagnetism on Co-doped CeO_2 nanoparticles: Mechanism and electronic and optical properties, *J. Phys. Chem. C* 118 (2014) 27039–27047.
- [24] Z.L. Wang, G.R. Li, Y.N. Ou, Z.P. Feng, D.L. Qu, Y.X. Tong, Electrochemical deposition of Eu^{3+} -doped CeO_2 nanobelts with enhanced optical properties, *J. Phys. Chem. C* 115 (2010) 351–356.
- [25] X.J. Wang, Q. Wang, F.T. Li, W.Y. Yang, Y. Zhao, Y.J. Hao, S.J. Liu, Novel $\text{BiOCl-C}_3\text{N}_4$ heterojunction photocatalysts: In situ preparation via an ionic-liquid-assisted solvent-thermal route and their visible-light photocatalytic activities, *Chem. Eng. J.* 234 (2013) 361–371.
- [26] X.Z. Li, H.Y. Shi, X.Y. Yan, S.X. Zuo, Y.Y. Zhang, Q. Chen, C. Yao, C.Y. Ni, Rational construction of direct Z-scheme doped perovskite/palygorskite nanocatalyst for photo-SCR removal of NO: Insight into the effect of Ce incorporation, *J. Catal.* 369 (2019) 190–200.
- [27] T. Taniguchi, T. Watanabe, N. Sugiyama, A.K. Subramani, H. Wagata, N. Matsushita, M. Yoshimura, Identifying defects in ceria-based nanocrystals by UV resonance Raman spectroscopy, *J. Phys. Chem. C* 113 (2009) 19789–19793.
- [28] A. Bueno-López, K. Krishna, M. Makkee, J.A. Moulijn, Enhanced soot oxidation by lattice oxygen via La^{3+} -doped CeO_2 , *J. Catal.* 230 (2005) 237–248.
- [29] J. Ke, J.W. Xiao, W. Zhu, H. Liu, R. Si, Y.W. Zhang, C.H. Yan, Dopant-induced modification of active site structure and surface bonding mode for high-performance nanocatalysts: CO oxidation on capping-free (110)-oriented CeO_2 : Ln ($\text{Ln} = \text{La-Lu}$) nanowires, *J. Am. Chem. Soc.* 135 (2013) 15191–15200.
- [30] J. Carey, M. Nolan, Dissociative adsorption of methane on the Cu and Zn doped (111) surface of CeO_2 , *Appl. Catal. B-Environ.* 197 (2016) 324–336.
- [31] S. Phanichphant, A. Nakaruk, D. Channei, Photocatalytic activity of the binary composite $\text{CeO}_2/\text{SiO}_2$ for degradation of dye, *Appl. Surf. Sci.* 387 (2016) 214–220.
- [32] J. Cheng, S. Huang, Y. Li, T.Q. Wang, L. Xie, X.C. Lu, RE (La, Nd and Yb) doped CeO_2 abrasive particles for chemical mechanical polishing of dielectric materials: Experimental and computational analysis, *Appl. Surf. Sci.* 506 (2020) 144668.
- [33] Y. Chen, C.Z. Zuo, Z.F. Li, A.L. Chen, Design of ceria grafted mesoporous silica composite particles for high-efficiency and damage-free oxide chemical mechanical polishing, *J. Alloy Compd.* 736 (2018) 276–288.
- [34] A.L. Chen, W.Y. Wang, X.Y. Ma, Y. Chen, Ceria coated hexagonal mesoporous silica core-shell composite particle abrasives for improved chemical-mechanical planarization performance, *J. Porous Mat.* 26 (2019) 1005–1015.
- [35] Y. Chen, A.L. Chen, J.W. Qin, Z.F. Li, Preparation of submicrometer mesoporous silica microspheres and fitting calculation for elastic moduli, *Chin. J. Nonferr. Metal* 27 (2017) 1228–1235 (In Chinese).
- [36] Y. Chen, C. Qian, N.M. Miao, Atomic force microscopy indentation to determine mechanical property for polystyrene-silica core-shell hybrid particles with controlled shell thickness, *Thin Solid Films* 579 (2015) 57–63.
- [37] X. Cao, G. Pan, P. Huang, D. Guo, G. Xie, Silica-coated core-shell structured polystyrene nanospheres and their size-dependent mechanical properties, *Langmuir* 33 (2017) 8225–8232.
- [38] H.S. Lee, H.D. Jeong, D.A. Dornfeld, Semi-empirical material removal rate distribution model for SiO_2 chemical mechanical polishing (CMP) processes, *Precis. Eng.* 37 (2013) 483–490.
- [39] Y.G. Wang, Y. Chen, F. Qi, D. Zhao, W.W. Liu, A material removal model for silicon oxide layers in chemical mechanical planarization considering the promoted chemical reaction by the down pressure, *Tribol. Int.* 93 (2016) 11–16.
- [40] X.J. Wen, C.G. Niu, L. Zhang, C. Liang, G.M. Zeng, A novel $\text{Ag}_2\text{O}/\text{CeO}_2$ heterojunction photocatalysts for photocatalytic degradation of enrofloxacin: possible degradation pathways, mineralization activity and an in-depth mechanism insight, *Appl. Catal. B-Environ.* 221 (2018) 701–714.